A new persistent luminescence phosphor of $ZnGa_2O_4:Ni^{2+}$ for the second near-infrared transparency window

Minghui Jin[1], Fan Li[1], Junqing Xiahou[1], Lin Zhu[2], Qi Zhu[1*] and Ji-Guang Li[3]

[1]*Key Laboratory for Anisotropy and Texture of Materials (Ministry of Education), School of Materials Science and Engineering, Northeastern University, Shenyang, Liaoning 110819, PR China*

[2]*College of Sciences, Northeastern University, Shenyang Liaoning 110819, PR China*

[3]*Research Center for Functional Materials, National Institute for Materials Science, Namiki 1-1, Tsukuba, Ibaraki 305-0044, Japan*

[*]Corresponding author:

Dr. Qi Zhu (Professor)

Tel: +86-24-8367-2700

E-mail: zhuq@smm.neu.edu.cn

Abstract

Recently, near-infrared (NIR) persistent phosphors become a research hotspot in biomedical application, because of their rather low absorption coefficients of biological tissues for NIR light. Most investigated phosphors emit NIR lights, whose wavelengths are no more than 1000 nm and located in NIR-I biological window. However, the phosphors emitting NIR lights in second (NIR-II, 1000-1350 nm) and third (NIR-III, 1500-1800 nm) biological window have advantages over that in NIR-I one. Here, persistent luminescent phosphors of $ZnGa_2O_4$:$x$$Ni^{2+}$ (x = 0-0.01) were synthesized *via* a traditional high-temperature solid-state reaction, which feature a broad emission band in the second near-infrared (NIR-II) window. Ni^{2+} tends to occupy Ga^{3+} site in $ZnGa_2O_4$, which results in the formation of oxygen vacancy. Upon ultraviolet (UV) or orange-red lights excitation, the phosphors exhibit a broad NIR emission at about 1300 nm, arising from the $^3T_2(^3F)\rightarrow{}^3A_2(^3F)$ transition of Ni^{2+}. Removing the light source yields intense NIR afterglow, with the duration longer than 500 s. Strongest NIR emission and best persistent luminescence are found for the x = 0.005 sample, which is excited by 254-nm UV light. The $ZnGa_2O_4$:Ni^{2+} persistent phosphors have potential application in vivo imaging, because of their charming emissions and afterglows with the wavelength locating in NIR-II window.

Keywords: Biological window; Ni^{2+}; Near-infrared; Persistent phosphors; $ZnGa_2O_4$

1. Introduction

Research has shown that hemoglobin, water and lipids are the main light-absorbing substances in biological tissues [1]. These substances have the lowest absorption coefficients for near-infrared (NIR) light with a wavelength of 650-1000 nm, which could penetrate into deep tissue and is referred to as the "bio-optical imaging window" [1]. Because of this, the NIR light has quickly become an attractive optical region for various biomedical applications [2], night-vision surveillance [3], anti-counterfeiting security [4] and antibacterial therapy [5, 6]. However, due to the further scientific investigation, researchers have found that the lights with the wavelengths exceeding 1000 nm, which are second (NIR-II, 1000-1350 nm) and third (NIR-III, 1500-1800 nm) biological windows, have advantages over the light with shorter wavelength [7]. The advantages of the light in NIR-II region are driving a growing number of researches on the phosphors emitting NIR-II light, such as rare-earth nanoparticles [8, 9], polymer nanomaterials [10], and aggregation-induced-emission (AIE) dots [11, 12].

Long persistent luminescent materials are also called light-storing luminescent materials and luminous materials [13]. They can absorb, store and slowly emit electromagnetic waves such as visible light, ultraviolet light, and even X-rays. As their most prominent feature, the afterglow duration of persistent luminescent materials can be about several seconds to hours, so they are widely used in lighting, marking [14], information storage [15], 3D printing [16], and etc. Since Matsuzawa et al. reported the green emitting long afterglow material of $SrAl_2O_4:Eu^{2+},Dy^{3+}$ in 1996 [17], a milestone work, the long afterglow material has attracted extensive attentions from researchers. At present, the anti-piracy technology based on visible light is facing the challenge of low security and inconvenience. However, the near-infrared long persistent luminescent materials have shown great potential in anti-counterfeiting technology [4, 18, 19] due to the characteristics of continuous outputs and invisible to the naked eye. Therefore, the research of new near-infrared long persistent luminescence materials has become a crucial part.

$ZnGa_2O_4$, an oxide compound with a spinel structure, belongs to the cubic crystal system with an optical band gap about 4.4 eV [20, 21]. It also has the characteristics of

excellent thermal and chemical stability, and its preparation process is simple, green and safe [22], which makes it be a good host for near-infrared light-emitting materials by doping activated ions, such as Cr^{3+}, Mn^{2+}, Ni^{2+}, Eu^{3+} [23-26] etc. The incorporation of transition metal ions in the host lattice may enhance the radiative transitions and luminescent properties [27-29]. For example, Cr^{3+}-doped zinc gallium ($ZnGa_2O_4:Cr^{3+}$) is a new promising phosphor that can convert ultraviolet/visible light to persistent NIR afterglow at ~700 nm [23, 30-32], and has been found broad application in biological imaging [33, 34], anti-counterfeiting technology [35] and even temperature measurement [32].

Ni^{2+} ions have strong absorption for ultraviolet and visible light. Under the excitation of ultraviolet light, Ni^{2+} in an octahedral coordination environment, has *d-d* electronic transitions originating from $^3T_2(^3F) \rightarrow {}^3A_2(^3F)$ [36, 37], so an ultra-broadband near-infrared light emission centered around 1300 nm will be found, which covers the whole NIR-II window. In addition, Ni^{2+}-doped zinc gallium ($ZnGa_2O_4:Ni^{2+}$) could output NIR afterglow, due to the unequal valence substitution [38]. However, most of the current reports on $ZnGa_2O_4:Ni^{2+}$ have revolved around the preparation and properties of transparent glass-ceramics [39-45], and few reports on powders and particles, which are very important for biomedical applications.

In this work, $ZnGa_2O_4:xNi^{2+}$ (x = 0-0.01) phosphors were synthesized by a traditional high-temperature solid-state reaction method. The synthesized samples were characterized by a series of techniques, such as X-ray diffraction (XRD), X-ray photoelectron spectroscopy (XPS), electron paramagnetic resonance (EPR), ultraviolet-visible-near-infrared (UV-Vis-NIR) spectroscopy, photoluminescence excitation/photoluminescence (PLE/PL) spectroscopy, thermo-luminescence (TL), and persistent luminescence decay analysis. The crystal structure, luminescence behavior, and persistent luminescence of the prepared samples were discussed in detail. The prepared $ZnGa_2O_4:Ni^{2+}$ phosphor with a broadband emission centered at about 1310 nm, which covers the second biological window (NIR-II), has a wide application in biological imaging. For a concise description, all acronyms are listed in Table S1.

2. Experimental Section

2.1. Materials and Synthesis

$ZnGa_2O_4$:$x$$Ni^{2+}$ (x = 0-0.01) phosphor powders (termed as ZGO:$x$$Ni^{2+}$ in the following content) were prepared by a conventional high-temperature solid-state reaction. The raw materials (ZnO, Ga_2O_3, and NiO) were all purchased from Sinopharm (Shanghai, China) with a high purity of 99.9%. All the raw materials were calculated accurately according to the stoichiometric ratio and weighed precisely by electronic balance. The materials were ground for 30 min in order to be fully mixed. The powder mixture was then pre-sintered at 1000 ^oC for 4 h in air. After being ground for 30 min again, the samples were finally placed in a tubular furnace and sintered at 1350 ^oC in air for 8 h. The samples were slowly cooled to room temperature and grinded for further test.

2.2. Characterization

The X-ray diffraction (XRD, Model SmartLab, Rigaku, Tokyo, Japan) patterns of the samples were recorded to analyze the phase identification, operating at 40 mA and 40 kV using nickel-filtered Cu Kα1 radiation and scanning with a speed of $10^o/2\theta$ from 10^o to 70^o. While the data for Rietveld refinement were recorded through the step-scan mode, using a step of 0.02^o and a counting time of 0.9 s per step, with the 2θ range from 15^o to 120^o. The photoluminescence spectrum (PL)/photoluminescence excitation spectrum (PLE) and persistent luminescence decay curves of Ni^{2+} were recorded using a model JY FL3-21 spectrofluorometer (Horiba, Kyoto), whereas a lamp capable of emitting light at 254, 302, and 365 nm was used for 6-minute excitation of samples prior to the persistent luminescence test. Thermoluminescence (TL) glow curves were obtained using a FJ-427A TL spectrofluorometer (Beijing Nuclear Instrument Factory) at a heating rate of 1 K s^{-1}, and the samples were exposed to the 254/302/365 nm UV light for 6 min before testing. The diffuse reflectance spectra of samples were measured by a UV-vis-NIR spectrophotometer (UV-3600 Plus, Shimadzu, Kyoto) in the spectral range of 200-800 nm at room temperature with $BaSO_4$ as a reference. X-ray photoelectron spectroscopy (XPS, Model Axis Supra, Shimadzu-Kratos Analytical Ltd.,

Manchester, U.K.) data were measured by monochromatized Al Kα X-ray radiation (1486.6 eV). The electron paramagnetic resonance (EPR) spectra of the samples were obtained using an EPR spectrometer (JES-FA 200, JEOL, Kyoto) with an X-band power of 9.063 GHz at room temperature.

2.3. Computational Details

The calculations were carried out using density functional theory (DFT), as implemented in the Vienna ab initio Simulation Package (VASP). The generalized gradient approximation (GGA) of the Perdew, Burke, and Ernzerhof (PBE) functional was used to treat the exchange correlations. The energy cut-off for the plane-wave basis set was kept at a fixed value of 520 eV. Structure optimization was accomplished until the force on each atom was less than 0.01 eV $Å^{-1}$. For the convenience of calculation, the ideal crystal of $ZnGa_2O_4$ is denoted as $Zn_8Ga_{16}O_{32}$ and $ZnGa_2O_4$ with one oxygen vacancy is denoted as $Zn_8Ga_{16}O_{31}$. On this basis, the related formation energy can be calculated by the following formula:

$$\Delta E_f(Zn_8Ga_{16}O_{31}) = (E(Zn_8Ga_{16}O_{31}) - E(Zn_8Ga_{16}O_{32}))/8 \quad (1)$$

The formation energy of Ni-doped samples is calculated by the following formula:

$$\Delta E_f(\text{Doped}) = (E(\text{Doped}) - E(Zn_8Ga_{16}O_{31}) + aE(Zn) + bE(Ga) - (a+b)E(Ni))/8 \quad (2)$$

When Ni occupies Zn site, the values are $a = 2$, $b = 0$; when Ni occupies Ga site, the values are $a = 0$, $b = 2$.

3. Results and Discussion

3.1. Phase Identification and Crystal Structure

It is known that the occupancy of Ni^{2+} is of importance to its luminescent properties and the tendency of the site occupied by Ni^{2+} can be judged by calculating the formation energy. It can be inferred that the oxygen vacancies ($V_O^{\bullet\bullet}$) may be formed during the high temperature solid state reaction, so we calculate the formation energy with different doping contents to clarify the occupancy of Ni^{2+} on the basis of considering the existence of oxygen defects in $ZnGa_2O_4$. The formation energy (ΔE_f) of $ZnGa_2O_4$

with one oxygen vacancy is calculated by the following formula:

$$\Delta E_f = E(V_O^{\bullet\bullet}) - E(\text{Perfect}) \quad (3)$$

where E(Perfect) represents the DFT total energy of the $ZnGa_2O_4$ perfect supercell and $E(V_O^{\bullet\bullet})$ represents the DFT total energy of the supercell with one oxygen vacancy. This formation energy was calculated to be 0.655 eV. The formation energy of Ni-doped samples is calculated by the following formula:

$$\Delta E_f = E(\text{Doped}) - E(V_O^{\bullet\bullet}) + \mu \quad (4)$$

where E(Doped) represents the DFT total energy of the unit cell with one Ni ion doping. Table 1 demonstrates the calculated formation energies of Ni doping in $ZnGa_2O_4$, which indicates that Ni^{2+} is more likely to replace Ga^{3+}, because of the lower formation energy of -0.059 eV. In a word, Ni^{2+} is more likely to occupy Ga^{3+} site in $ZnGa_2O_4$, forming a six-coordinated octahedron. The calculated results are in good agreement with the reported literature [46].

Table 1

The calculated formation energies (ΔE_f) of Ni^{2+} doping.

	E(Doped)	$E(V_O^{\bullet\bullet})$	ΔE_f	μ
Ni-Zn	-304.725 eV	-303.120 eV	-0.008 eV	1.597 eV
Ni-Ga	-301.448 eV	-303.120 eV	-0.059 eV	-1.731 eV

As the result shown in Table 1, Ni^{2+} ions tend to occupy the Ga^{3+} sites, which is also mainly due to the similar ionic radii between Ni^{2+} (0.69 Å for six-coordination) and Ga^{3+} (0.62 Å for six-coordination) ions. The crystal structure is shown in Fig. 1a. Fig. 1b shows the XRD patterns of ZGO:$x$$Ni^{2+}$ phosphors, and it can be seen that all diffraction peaks of the samples are in good agreement with the data in $ZnGa_2O_4$ standard card JCPDS No. 38-1240, indicating that single-phase samples have been obtained. The diffraction peaks of the sample are very sharp and intense, indicating a high degree of crystallinity. The powder diffraction data of the ZGO:$x$$Ni^{2+}$ (x = 0, 0.001, and 0.01) were also analyzed via Rietveld refinement using the TOPAS software. Fig. 1c-e show the results of profile fitting. By comparing the calculated data with experimental patterns finds that all the peaks are indexed by the cubic cell (*Fd*3m) with

the parameters being close to that of $ZnGa_2O_4$ (spinel-type structure). Rietveld refinements also show the stable and acceptable reliability factors, further indicating that the samples are single phase.

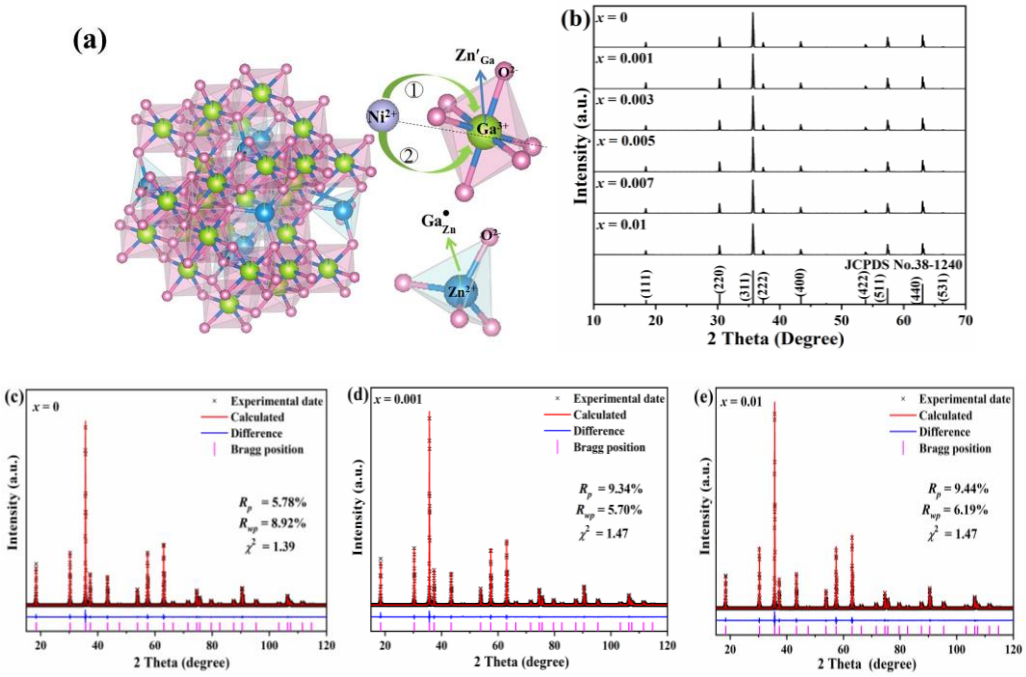

Fig. 1. (a) Crystal structure, (b) XRD patterns of ZGO: xNi^{2+} samples (x = 0, 0.001 0.003, 0.005, 0.007, 0.01) and (c-e) Rietveld refinement of ZGO: xNi^{2+} samples (x = 0, 0.001, 0.01).

The valence states of the Ni ions are analyzed by the Ni 2p core-level XPS spectra. Fig. 2a shows the high-resolution spectrum of Ni $2p_{3/2}$, and the binding energies are corrected for the charging effect with the reference of the C 1s line at 284.8 eV [39, 47, 48]. As depicted in the spectrum, the main Ni $2p_{3/2}$ peak is located at 855.2 eV and another peak at 861.2 eV is typically assigned to its satellite [39]. All these peaks are very close to that of Ni^{2+} ions, revealing that that the valence state of the Ni ions in the sample is +2 and Ni^{2+} ions are successfully doped into $ZnGa_2O_4$. Meanwhile, we know that the value of g in electron paramagnetic resonance (EPR) measurement is the primary empirical parameter that characterizes the response of a paramagnetic molecule [49]. The signals at about g_1 = 2.21 and g_2 = 1.99 appear in the EPR spectra of all samples (Fig. 2b), implying the existence of Ni^{2+} ions and $V_O^{\bullet\bullet}$, respectively [49-52].

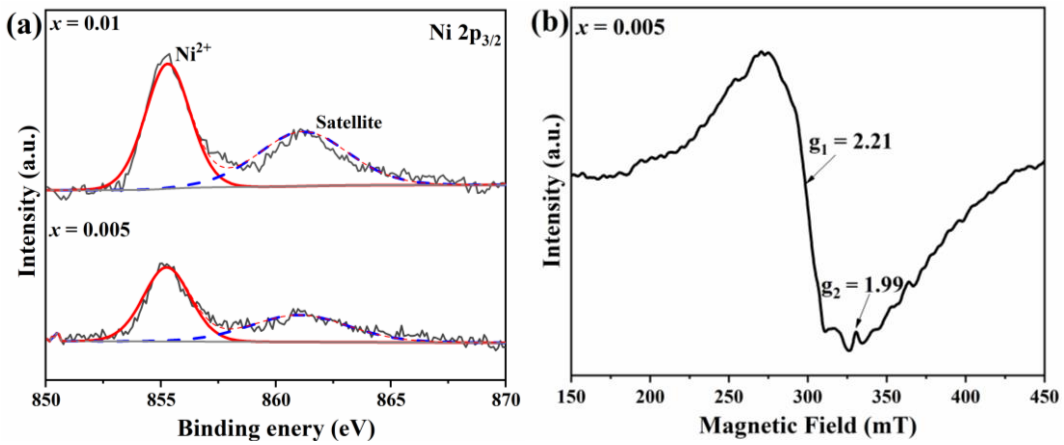

Fig. 2. (a) Ni 2p core-level of ZGO:xNi^{2+} samples (x = 0.005, 0.01) and (b) Room-temperature (298 K) X-band EPR spectra of ZGO:0.005Ni^{2+} after 10 min-UV excitation (λ_{ex} = 365 nm).

3.2. Luminescence Properties

Fig. 3a shows the diffuse reflectance (DR) spectra of ZGO:xNi^{2+} samples (x = 0 ,0.005, 0.01). It can be seen that there are two spin-allowed transition peaks at about 380 nm and 610 nm, arising from the $^3A_2(F)\rightarrow{}^3T_1(P)$ and $^3A_2(F)\rightarrow{}^3T_1(F)$ transitions of Ni^{2+} in the octahedral structure, respectively [40, 55]. The peak centered at about ~250 nm comes from the charge transfer band (CTB) of Ga^{3+}-O^{2-} [30]. These peaks can also be observed in the latter photoluminescence excitation (PLE) spectra. Because the host absorption of $ZaGa_2O_4$ is close to the charge transfer band, the strong band could the overlap charge transfer band and the host absorption band.

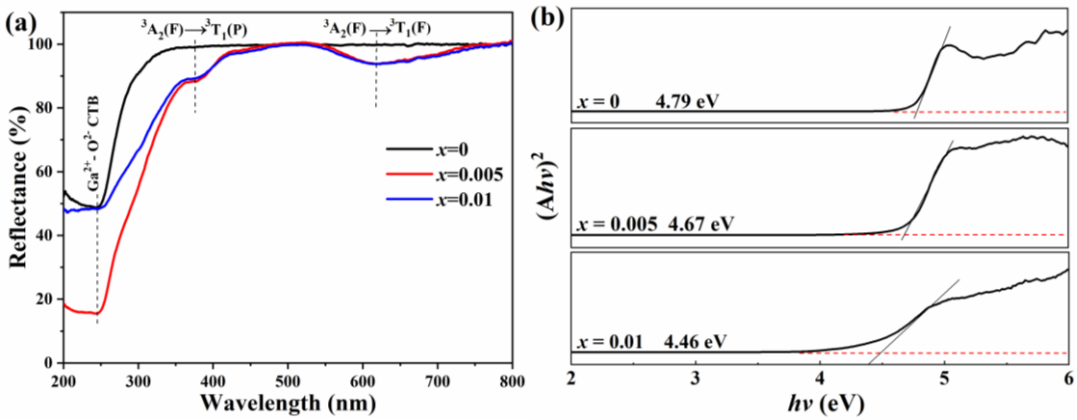

Fig. 3. (a) Diffuse reflectance spectra and (b) Band-gap energies for ZGO:xNi (x = 0,

0.005, 0.01) samples.

In order to estimate the optical band gap, the diffuse reflection of the samples is converted to Kubelka−Munk function $F(R_\infty)$, and the formula is as follows [56, 57]:

$$F(R_\infty) = (1\text{-}R)^2/(2\times R) = K/S \quad (5)$$

where R is the reflection coefficient, K is absorption coefficients, and S is the scattering coefficient. As an approximate value, the diffusion coefficient is independent on wavelength, and then $(h\nu\times F(R_\infty))^2$–$h\nu$ diagram is drawn according to the expression proposed by A. Escobedo Morales [58], and the expression is as follows:

$$(h\nu\times F(R_\infty))^2 = A\times(h\nu\text{-}E_g) \quad (6)$$

where $h\nu$ represents the photo energy, A represents a proportional constant, Eg represents the value of bandgap. The band gap energy of the samples is shown in Fig. 3b. This value can be read out from the intercept of the fitted straight line. Through the liner fitting method, the E_g value is calculated to be ~4.79 eV for x = 0. Increasing the x value from 0 to 0.1 results in the E_g value gradually decreases from ~4.79 to 4.46 eV. Meanwhile, the partial and total density of states of the samples are calculated in Fig. 4. The value of the calculated bandgap is smaller than the experimental one, which is expected since the GGA (generalized gradient approximation) underestimates the size of the bandgap [32, 35, 59]. The result also indicates that the band gap energy of the samples becomes narrower from ~4.00 eV to 3.68 eV by incorporation of Ni^{2+} ions. More ions doping would contribute to more defects, which results in defect energy levels below the conduction band bottom (CBB). When there are defect energy levels in the band gap, the band gap will gradually decrease [60].

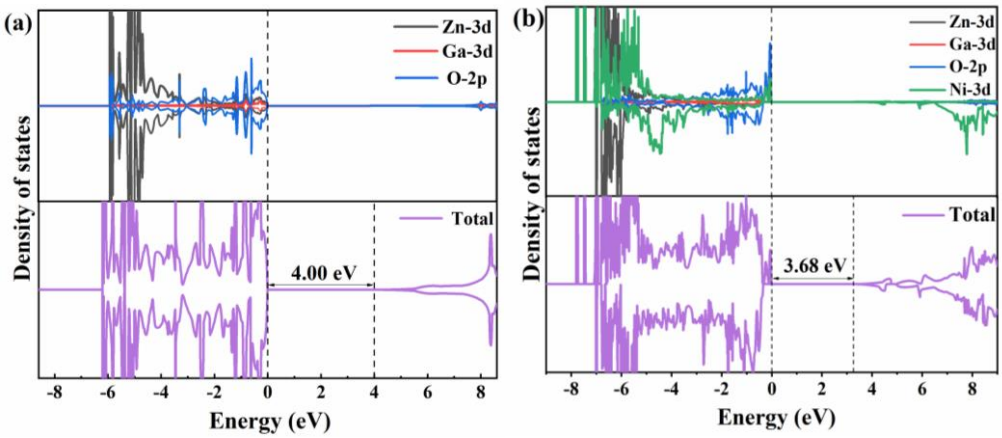

Fig. 4. Partial and total density of states of (a) $Zn_8Ga_{16}O_{31}$ and (b) $Zn_8Ga_{14}O_{31}Ni_2$.

To analyze the luminescence properties, photoluminescence excitation (PLE) and photoluminescence (PL) spectra of the ZGO:xNi^{2+} spinel phosphors were performed. Fig. 5a and 5b display PLE spectra of the ZGO:xNi^{2+} samples calcined at 1350 °C. It can be seen that the spectra contain three main excitation bands monitored at 1310 nm. The strong excitation band ranging from 220 to 350 nm is assigned to an overlap of two peaks, which are a weaker one centered at ~260 nm assigned to the Ga^{3+}-O^{2-} charge transfer (CT) and another strong band with maxima at 300-350 nm assigned to the Ni^{2+}-O^{2-} charge transfer [54]. Meanwhile, the band centered at ~380 nm can be assigned to the $^3A_2(F)\rightarrow{}^3T_1(P)$ transition of Ni^{2+}. In addition, there is a relatively weak peak centered at ~602 nm which can be assigned to the $^3A_2(F)\rightarrow{}^3T_1(F)$ transition of Ni^{2+}. Therefore, the samples can not only be excited by ultraviolet (UV) light but also by orange-red light (Fig. 5d), which is a more safe excitation light for human body. For charge transfer excitation, the O^{2-} 2p electrons are excited into the 3d levels of Ni^{2+} and Ga^{3+}, and the position of the CT band is determined by the energy difference between the O^{2-} 2p valence band and the 3d levels of Ni^{2+} and Ga^{3+}. The obvious red shifts are found for the CT band center position of Ga-O from ~269 nm to ~320 nm, and the CT band center position of Ni-O from ~302 nm to ~321 nm, indicating a decreased energy difference. It is known that the higher valence state of the ions, the stronger their attraction for electrons of orbits of other ions, and the larger electronegative they are. The red-shift of CT band is due to the different value of the electronegativity (EN)

between Ni^{2+} (EN = 1.367) and Ga^{3+} (EN = 1.579) [61]. With the increase of Ni^{2+} content, the overall electronegativity of the sample decreases, so the energy required for the whole CT excitation process becomes smaller and thus the band positions of Ni-O and Ga-O are red-shifted.

Compared with the intensity of the excitation peak at ~260 nm, we can see that the intensity of the excitation peaks at ~380 nm increases with increasing the doping amount of the Ni^{2+} ions (the *x* value). However, the intensity of the excitation peaks at ~310 nm increases faster at the beginning, and it reaches the maximum value at x = 0.005. Then the intensity decreases at a higher *x* value (Fig. 5b). The similar law is observed in the PL spectra for the samples excited by 310 nm (Fig. 5c). It can be inferred that the luminescence quenching concentration of Ni^{2+} ions is at x = 0.005. When excited by 310 nm, all samples exhibit NIR emission with two peaks centered at about 1276 nm and 1310 nm, which are resulted from the $^3T_2(^3F) \rightarrow {}^3A_2(^3F)$ transition of Ni^{2+}. There are anti-site defects in the $ZnGa_2O_4$ matrix, therefore, two kinds of local environments for Ni^{2+} ions (octahedral site) exist in $ZnGa_2O_4$ [62]. Ni^{2+} ions occupy the Ga^{3+} ions site (octahedral site), so part of Ni^{2+} ions may occupy the Ga^{3+} ions site and are adjacent to the anti-site defects, while others are away from the anti-site defects. Therefore, the different site distributions of Ni^{2+} may contribute to the broad emission band. The intensity ratio of $I_{1310\ nm}/I_{1276\ nm}$ (the inset of Fig. 5c) gradually increases with the incorporation of Ni^{2+} ions. Because the anti-site defects in $ZnGa_2O_4$ is only 3at% [19], more incorporation of Ni^{2+} ions would lead to more Ni^{2+} ions occupying the Ga^{3+} sites away from the anti-site defects. Therefore, the peak at 1310 nm can be assigned to the emission of the Ni^{2+} ions normally occupying the Ga^{3+} ions sites and the other one at 1276 nm can be assigned to the emission of the Ni^{2+} ions that are adjacent anti-site defects. The luminance of x = 0.005 sample is estimated to be ~115 mcd/m^2, through comparing its integrated intensity to that of the commercial phosphor $SrAl_2O_4:Eu^{2+},Dy^{3+}$ [63, 64].

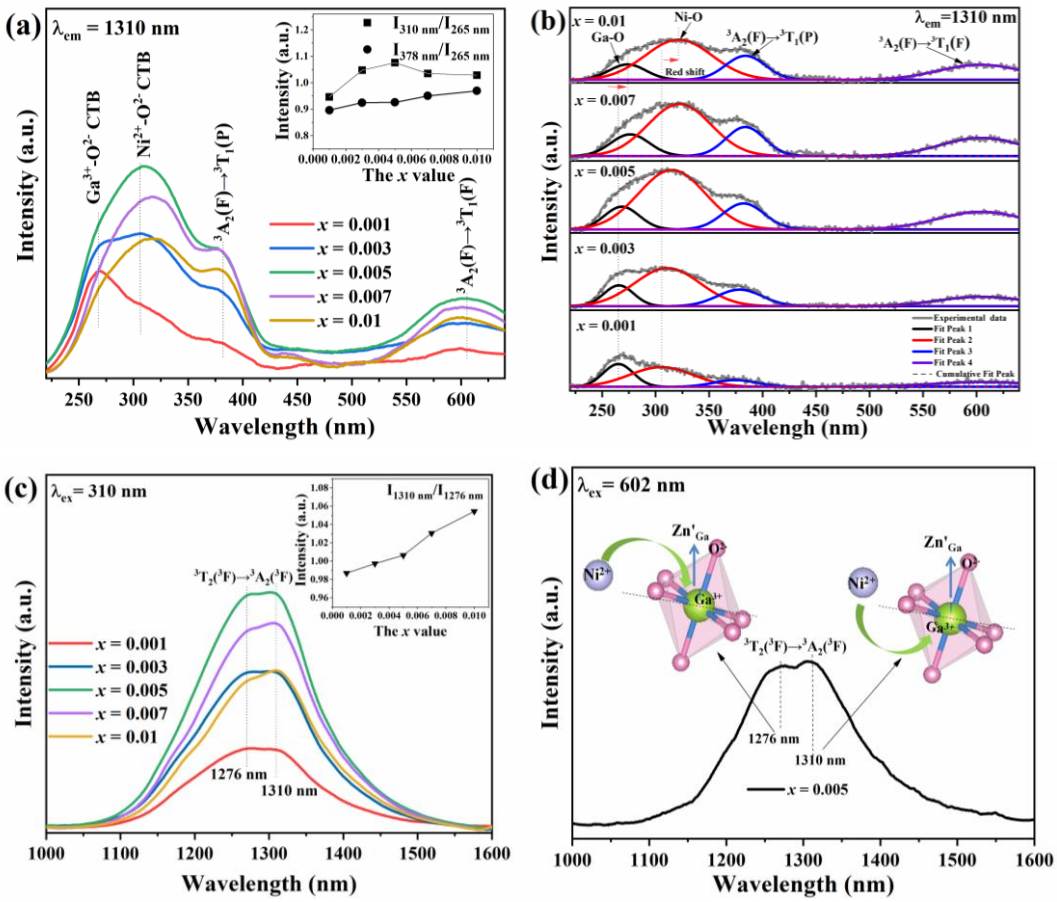

Fig. 5. (a) PLE spectra and (b) Gaussian fitting PLE spectra of ZGO:*x*Ni monitored at 1310 nm, (c) PL spectra of ZGO:*x*Ni excited by 310 nm and (d) PL spectra of ZGO:0.005Ni excited by 602 nm. The insets in (a) and (c) are the intensity ratios of $I_{310\ nm}/I_{265\ nm}$, $I_{374\ nm}/I_{265\ nm}$ and $I_{1310\ nm}/I_{1276\ nm}$.

The prepared samples can exhibit intense NIR afterglow after being exposed to UV-light irradiation. The NIR afterglow decay curves of ZGO:0.005Ni^{2+} sample are displayed in Fig. 6a, which confirms that the NIR afterglow of all samples can last at least 500 s after exposure to the UV light for 6 min. This is mainly due to that the afterglow luminance at 500 s is estimated to be higher than 0.87 mcd/m^2, which is greater than the value of 0.32 mcd/m^2 [63]. In addition, the sample exhibits the best persistent luminescence after excitation with 254-nm UV light, since the 254-nm UV light with the highest energy can make all the electron traps be fully filled. It is believed that electron traps play a great important role on persistent luminescence, and the distribution and the number of traps are the key factors [32, 65, 66]. After removing the

excitation light, the electrons will escape from the traps and jump into the energy level of the luminescence center with a thermal disturbance, thus resulting in the afterglow. Therefore, the TL measurement of the sample is used to analyze the traps of the sample. Fig. 6b-d show the Gaussian fitting TL glow curves for the ZGO:0.005Ni^{2+} sample. The approximate trap depth E can be estimated by the following equation [67]:

$$E = T_m/500 \quad (7)$$

where T_m is the temperature of the peak maximum in TL glow curves (kelvin temperature). We can see that there are two peaks for the sample's TL curves. Low and high temperature peaks (T_1 and T_2) correspond to shallow and deep traps, respectively. The two traps are formed by two different kinds of defects: one is the anti-site defects caused by Ga^{3+} replaced by Zn^{2+}; the other is the oxygen-vacancy defects formed by the replacing of Ni^{2+} for Ga^{3+}. The calculated electron-trap depths (E_1 and E_2) for the sample are shown in Table 2. For λ_{ex} = 254 nm, the calculated values are E_1 = 0.726 eV and E_2 = 0.832 eV; For λ_{ex} = 302 nm, the calculated values are E_1 = 0.710 eV and E_2 = 0.784 eV; For λ_{ex} = 365 nm, calculated values are E_1 = 0.670 eV and E_2 = 0.742 eV. As the wavelength of the UV excitation light source increases, the peaks of T_1 and T_2 shift to lower temperature and the E value decreases. During the same time period, the 254-nm excited sample has the strongest afterglow, but the 365-nm excited sample has the weakest afterglow (Fig. 6a). Higher-energy light excitation makes the traps be full filled with the excited electrons, both for the shallow and deep traps. However, lower-energy light excitation makes the traps be part filled, and the lower energy of the excitation light is the smaller the filling proportion is (Fig. 6e). Therefore, the phosphor excited by 254-nm exhibits the best persistent luminescence.

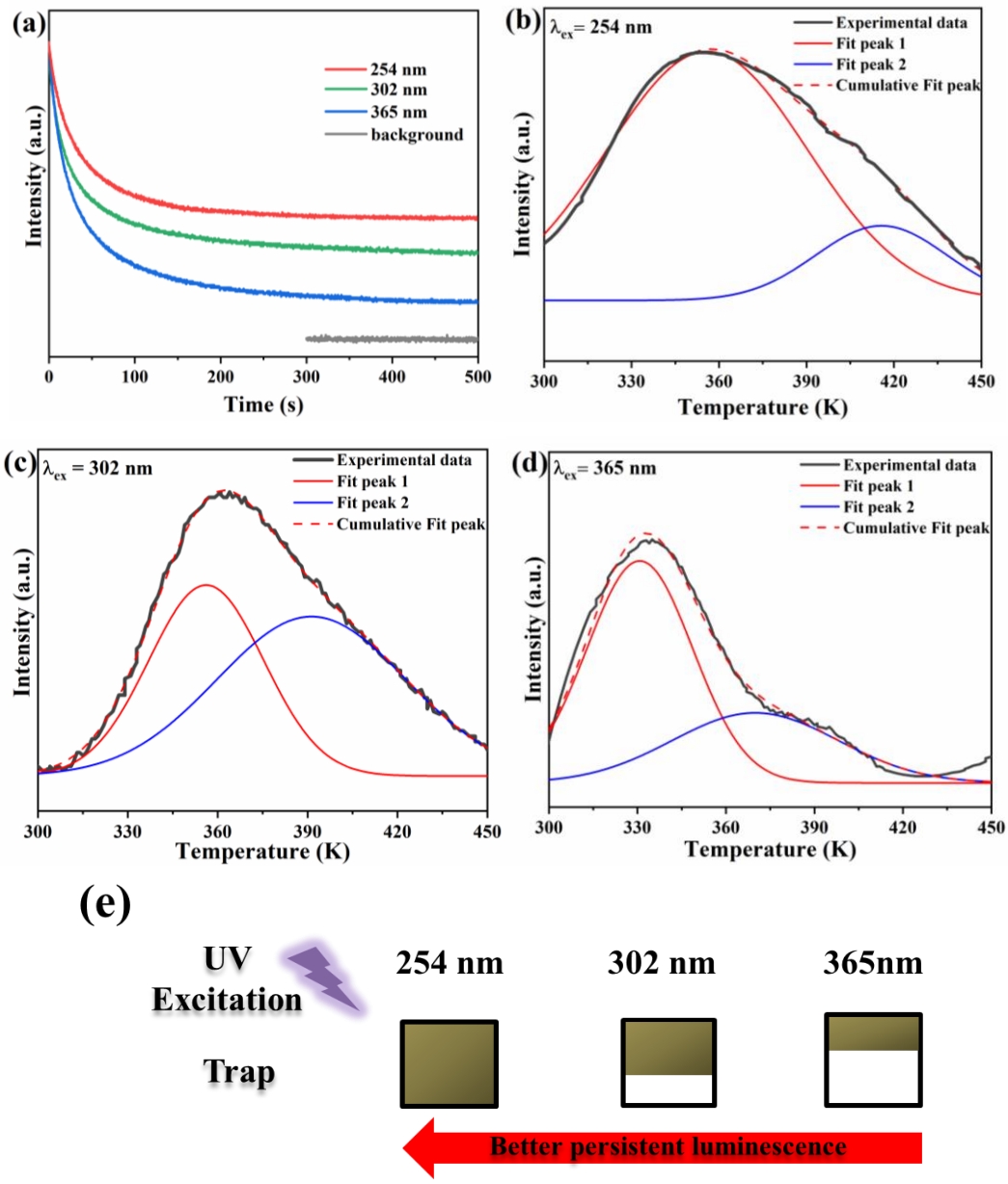

Fig. 6. (a) Persistent luminescence decay curves, (b-d) Thermo-luminescence (TL) curves and (e) Schematic diagram of the trap being filled with electrons for ZGO:0.005Ni^{2+} sample after 254-nm, 302-nm and 365-nm UV light illumination for 6 min.

Table 2

Calculated trap depths (E) of ZGO:0.005Ni^{2+}.

UV light/nm	T_1/K	T_2/K	E_1/eV	E_2/eV
254	358	416	0.726	0.832
302	355	392	0.710	0.784
365	333	371	0.670	0.742

Tanabe-Sugano diagram is used to interpret the emissions of transition metal ions (Fig. 7a). The crystal field parameters of Ni^{2+} were estimated from the absorption spectra according to the Tanabe-Sugano equations [68-70]:

$$D_q = \frac{v_1}{10} \tag{8}$$

$$B = \frac{(v_2-2v_1)(v_2-v_1)}{3(5v_2-9v_1)} \tag{9}$$

where D_q is the crystal field strength parameter, B is the electronelectron Racah parameter, and v_1 and v_2 are the energy of the $^3A_2(F)\rightarrow{}^3T_2(F)$ and $^3A_2(F)\rightarrow{}^3T_1(P)$ transitions, respectively. The ratio of $10D_q$ to B indicates the ligand field strength around the Ni^{2+} ion and the evaluated value of x = 0.005 sample from the above equations is $10D_q/B$ = 15.47. The related luminescence mechanism and persistent luminescence in this work can be derived from the Tanabe-Sugano diagram (Fig. 7b). Under the excitation of UV lamp, some electrons are excited from valence band (VB) to conduction band (CB), and some are excited from the ground state $^3A_2(^3F)$ of Ni^{2+} to energy levels of $^3T_1(^3F)$ and $^3T_1(^3P)$ of Ni^{2+}. Then the excited electrons return from CB, $^3T_1(^3F)$ and $^3T_1(^3P)$ to $^3T_2(^3F)$ energy level through non radiative transition, and the transition of electrons from $^3T_2(^3F)$ to $^3A_2(^3F)$ contributes to the NIR emissions. Besides, under the excitation of UV light, the electrons, promoted to conduction band (CB), could be captured by the electron traps near the CB and the electron traps are filled during a sufficient illumination time. After removing the UV light irradiation, recombination between the electrons released from the electron traps through conduction band and the excited energy levels of Ni^{2+} contributes to the NIR afterglows. The prepared $ZnGa_2O_4$:Ni^{2+} persistent phosphors are the potential materials for application in vivo imaging, due to their charming emissions and afterglows locating in NIR-II window [28].

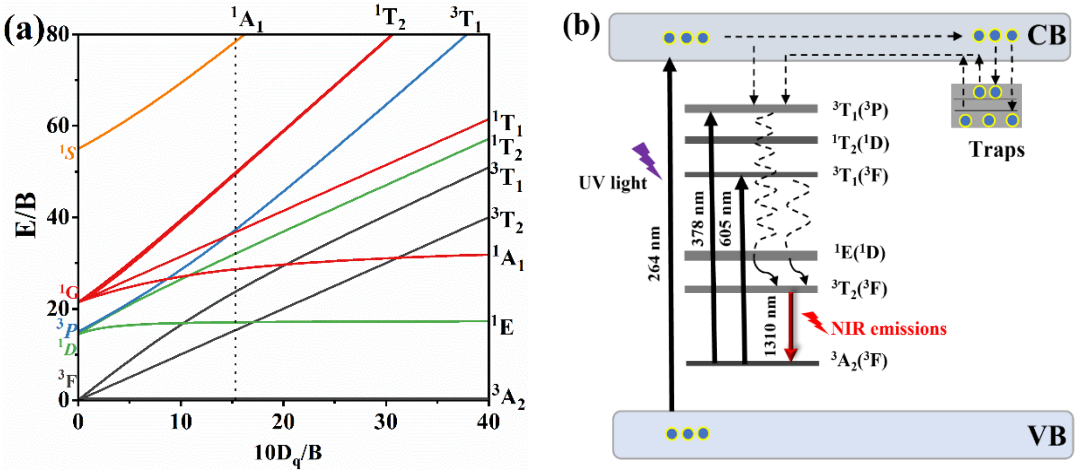

Fig. 7. (a) Tanabe–Sugano diagram of octahedral Ni^{2+} and (b) Schematic illustration for the luminescence mechanism of ZGO:Ni^{2+} phosphors.

4. Conclusions

In this work, we have successfully synthesized $ZnGa_2O_4$:xNi^{2+} (x = 0-0.01) persistent luminescent phosphors *via* a traditional high-temperature solid-state reaction, which feature a broad emission band in the second near-infrared (NIR-II) window. The samples were characterized by XRD, XPS, EPR, DFT calculations, UV-Vis-NIR, TL, PLE/PL spectroscopy, and persistent luminescence decay analysis. Ni^{2+} is more likely to occupy Ga^{3+} site in $ZnGa_2O_4$, forming a six-coordinated octahedron. The incorporation of Ni^{2+} ions leads to the formation of oxygen vacancies ($V_O^{\cdot\cdot}$), which contributes to a decrease of band gap and a red shift of charge transfer band (Ni-O and Ga-O). The samples can not only be excited by ultraviolet (UV) light but also by orange-red light, which exhibit a broad NIR emission at about 1310 nm ($^3T_2(^3F)\rightarrow{}^3A_2(^3F)$ transition of Ni^{2+}). After removing the light source, the sample outputs intense NIR afterglow, which can last more than 500 s. The x = 0.005 sample exhibits the strongest NIR emission, and the sample excited by 254-nm UV light outputs the best persistent luminescence. The prepared $ZnGa_2O_4$:Ni^{2+} persistent phosphors are the potential materials for application in vivo imaging, due to their charming emissions and afterglows with the wavelength locating in NIR-II window. However, the duration and intensity of the afterglow need to be further improved in the

future, because long lasting and intense NIR signals are necessary for the practical vivo imaging application.

Acknowledgements

This work was supported in part by the Natural Science Foundation of Liaoning Province (Grant 2020-MS-081), and National Natural Science Foundation of China (Grant 51302032).

References

[1] R. Weissleder, A clearer vision for in vivo imaging., Nat. Biotechnol. 19 (2001) 316.

[2] M.H. Chan, W.T. Huang, K.C. Chen, T.Y. Su, Y.C. Chan, M. Hsiao, R.S. Liu, The optical research progress of nanophosphors composed of transition elements in the fourth period of near-infrared windows I and II for deep-tissue theranostics, Nanoscale 14 (2022) 7123-7136.

[3] J. Battaglia, R. Brubaker, M. Ettenberg, D. Malchow, High speed short wave infrared (SWIR) imaging and range gating cameras, Proc. SPIE, 6541 (2007) 654106.

[4] C. Ma, H. Liu, F. Ren, Z. Liu, Q. Sun, C. Zhao, Z. Li, The second near-infrared window persistent luminescence for anti-counterfeiting application, Cryst. Growth Des. 20 (2020) 1859-1867.

[5] Y. Ding, Z. Yuan, J-W. Hu, K. Xu, H. Wang, P.Liu, K-Y.Cai, Surface modification of titanium implants with micro-nanotopography and NIR photothermal property for treating bacterial infection and promoting osseointegration, Rare Met. 41 (2022) 673-688.

[6] M. Z. Chai, M. W. An, X. Y. Zhang, P. K. Chu. In vitro and in vivo antibacterial activity of graphene oxide-modified porous TiO_2 coatings under 808-nm light irradiation, Rare Met. 41 (2022) 540-545.

[7] Y. Gao, B. Wang, L. Liu, K. Shinozaki, Near-infrared engineering for broad-band wavelength-tunable in biological window of NIR-Ⅱ and -Ⅲ: A solid solution phosphor of $Sr_{1-x}Ca_xTiO_3:Ni^{2+}$, J. Lumin. 238 (2021) 118235.

[8] D.J. Naczynski, M.C. Tan, M. Zevon, B. Wall, J. Kohl, A. Kulesa, S. Chen, C.M. Roth, R.E. Riman, P.V. Moghe, Rare-earth-doped biological composites as *in vivo* shortwave infrared reporters, Nat. Commun. 4 (2013) 2199.

[9] R. Wang, X. Li, L. Zhou, F. Zhang, Epitaxial seeded growth of rare-earth nanocrystals with efficient 800 nm near-infrared to 1525 nm short-wavelength infrared downconversion photoluminescence for in vivo bioimaging, Angew. Chem. 53 (2014) 12282-12286.

[10] K. Shou, Y. Tang, H. Chen, S. Chen, L. Zhang, A. Zhang, Q. Fan, A. Yu, Z. Cheng, Diketopyrrolopyrrole-based semiconducting polymer nanoparticles for in vivo second near-infrared window imaging and image-guided tumor surgery, Chem. Sci. 9 (2018) 3105-3110.

[11] Z. Xu, Y. Jiang, M. Fan, S. Tang, M. Liu, W.C. Law, C. Yang, M. Ying, M. Ma, B. Dong, K.T. Yong, G. Xu, Aggregation- induced emission nanoprobes working in the NIR- II region: From material design to fluorescence imaging and phototherapy, Adv. Opt. Mater. 9 (2021) 2100859.

[12] C. Li, Q. Wang, Challenges and opportunities for intravital near-infrared fluorescence imaging technology in the second transparency window, ACS Nano 12 (2018) 9654-9659.

[13] J. Hölsä, Persistent luminescence beats the afterglow: 400 years of persistent luminescence, Electrochem. Soc. Interface 18 (2009) 42-45.

[14] S. Liu, H. Cai, S. Zhang, Z. Song, Q. Liu, An emerging NIR super-long persistent phosphor and its applications, Mater. Today Chem. 24 (2022).

[15] K.V.d. Eeckhout, D. Poelman, P.F. Smet, Persistent luminescence in non-Eu^{2+}-doped compounds: A review, Materials 6 (2013) 2789-2818.

[16] M. Zhang, W. Zeng, Y. Lei, X. Chen, M. Zhang, C. Li, S. Qin, A novel sustainable luminescent ABS composite material for 3D printing, Eur. Polym. J. 176 (2022).

[17] T. Matsuzawa, Y. Aoki, N. Takeuchi, Y. Murayama, A new long phosphorescent phosphor with high brightness, $SrAl_2O_4$:Eu^{2+},Dy^{3+}, J. Electrochem. Soc. 143 (1996) 2670-2673.

[18] L. Lei, D. Chen, C. Li, F. Huang, J. Zhang, S. Xu, Inverse thermal quenching effect

in lanthanide-doped upconversion nanocrystals for anti-counterfeiting, J. Mater. Chem. C 6 (2018) 5427-5433.

[19] M. You, M. Lin, S. Wang, X. Wang, G. Zhang, Y. Hong, Y. Dong, G. Jin, F. Xu, Three-dimensional quick response code based on inkjet printing of upconversion fluorescent nanoparticles for drug anti-counterfeiting, Nanoscale 8 (2016) 10096-10104.

[20] Y. Zhang, Z. Wu, D. Geng, X. Kang, M. Shang, X. Li, H. Lian, Z. Cheng, J. Lin, Full color emission in $ZnGa_2O_4$: simultaneous control of the spherical morphology, luminescent, and electric properties via hydrothermal approach, Adv. Funct. Mater. 24 (2014) 6581-6593.

[21] L. Zou, X. Xiang, M. Wei, F. Li, D.G. Evans, Single-crystalline $ZnGa_2O_4$ spinel phosphor via a single-source inorganic precursor route, Inorg. Chem. 47 (2008) 1361-1369.

[22] J. Su, S. Ye, X. Yi, F.Q. Lu, X.B. Yang, Q.Y. Zhang, Influence of oxygen vacancy on persistent luminescence in $ZnGa_2O_4:Cr^{3+}$ and identification of electron carriers, Opt. Mater. Express 7 (2017) 734-743.

[23] M.K. Hussen, F.B. Dejene, G.G. Gonfa, Effect of citric acid on material properties of $ZnGa_2O_4:Cr^{3+}$ nanopowder prepared by sol–gel method, Appl. Phys. A: Mater. Sci. Process. 124 (2018) 390.

[24] G. Yu, W. Wang, C. Jiang, A new direction for transition metal ion doped cubic spinel-type oxides with broadband NIR emission., J. Lumin. 235 (2021) 118061.

[25] T. Si, Q. Zhu, J. Xiahou, X. Sun, J.-G. Li, Regulating Mn^{2+}/Mn^{4+} activators in $ZnGa_2O_4$ via Mg^{2+}/Ge^{4+} doping to generate multimode luminescence for advanced anti-counterfeiting, ACS Appl. Electron. Mater. 3 (2021) 2005-2016.

[26] C.P. Wang, Y.X. Zhang, X. Han, D.F. Hu, D.P. He, X.M. Wang, H. Jiao, Energy transfer enhanced broadband near-infrared phosphors: Cr^{3+}/Ni^{2+} activated $ZnGa_2O_4$-Zn_2SnO_4 solid solutions for the second NIR window imaging, J. Mater. Chem. C 9 (2021) 4583-4590.

[27] C.V. Reddy, R. Koutavarapu, R. Ravikumar, J. Shim, A novel green-emitting Ni^{2+}-doped Ca-Li hydroxyapatite nanopowders: structural, optical, and photoluminescence

properties, J. Mater. Sci. - Mater. Electron. 31 (2020) 5097-5106.

[28] M.K. Hossain, S. Hossain, M.H. Ahmed, M.I. Khan, N. Haque, G.A. Raihan, A Review on optical applications, prospects, and challenges of rare-earth oxides, ACS Appl. Electron. Mater. 3 (2021) 3715-3746.

[29] M.K. Hossain, M.H. Ahmed, M.I. Khan, M.S. Miah, S. Hossain, Recent progress of rare earth oxides for sensor, detector, and electronic device applications: A Review, ACS Appl. Electron. Mater. 3 (2021) 4255-4283.

[30] Z. Pan, Y.-Y. Lu, F. Liu, Sunlight-activated long-persistent luminescence in the near-infrared from Cr^{3+}-doped zinc gallogermanates, Nat. Mater. 11 (2011) 58-63.

[31] M. Allix, S. Chenu, E. Véron, T. Poumeyrol, E.A. Kouadri-Boudjelthia, S. Alahraché, F. Porcher, D. Massiot, F. Fayon, Considerable improvement of long-persistent luminescence in germanium and tin substituted $ZnGa_2O_4$, Chem. Mater. 25 (2013) 1600-1606.

[32] J. Xiahou, Q. Zhu, L. Zhu, S. Li, J.-G. Li, Local structure regulation in near-infrared persistent phosphor of $ZnGa_2O_4$:Cr^{3+} to fabricate natural-light rechargeable optical thermometer, ACS Appl. Electron. Mater. 3 (2021) 3789-3803.

[33] T. Maldiney, A. Bessiere, J. Seguin, E. Teston, S.K. Sharma, B. Viana, A.J. Bos, P. Dorenbos, M. Bessodes, D. Gourier, D. Scherman, C. Richard, The in vivo activation of persistent nanophosphors for optical imaging of vascularization, tumours and grafted cells, Nat. Mater. 13 (2014) 418-426.

[34] Q. Zhu, J. Xiahou, Y. Guo, H. Li, C. Ding, J. Wang, X. Li, X. Sun, J.-G. Li, $Zn_3Ga_2Ge_2O_{10}$:Cr^{3+} uniform microspheres: template-free synthesis, tunable bandgap/trap depth, and *in vivo* rechargeable near-infrared-persistent luminescence, ACS Appl. Bio Mater. 2 (2018) 577-587.

[35] J. Xiahou, Q. Zhu, L. Zhu, S. Huang, T. Zhang, X. Sun, J.-G. Li, Lattice-site engineering in $ZnGa_2O_4$:Cr^{3+} through Li^+ doping for dynamic luminescence and advanced optical anti-counterfeiting, J. Mater. Chem. C 10 (2022) 7935-7948.

[36] B.N. Samson, L.R. Pinckney, J. Wang, G.H. Beall, N.F. Borrelli, Nickel-doped nanocrystalline glass-ceramic fiber, Opt. Lett. 27 (2002) 1309-1311.

[37] S. Zhou, N. Jiang, B. Wu, J. Hao, J. Qiu, Ligand-driven wavelength-tunable and

ultra-broadband infrared luminescence in single-ion-doped transparent hybrid materials, Adv. Funct. Mater. 19 (2009) 2081-2088.

[38] G. Yu, W. Wang, C. Jiang, Linear tunable NIR emission via selective doping of Ni^{2+} ion into ZnX_2O_4 (X=Al, Ga, Cr) spinel matrix, Ceram. Int. 47 (2021) 17678-17683.

[39] L. Yang, Y. Zhao, R. Yin, F. Li, Synthesis of Ni^{2+}-doped $ZnAl_2O_4$/ZnO composite phosphor film with largely enhanced polychromatic emission via a single-source precursor, J. Am. Ceram. Soc. 97 (2014) 1123-1130.

[40] S. Zhou, G. Feng, B. Wu, J. Nan, S. Xu, J. Qiu, Intense infrared luminescence in transparent glass-ceramics containing β-Ga_2O_3:Ni^{2+} nanocrystals, J. Phys. Chem. C 111 (2007) 7335-7338.

[41] E.T. Basore, X. Liu, J. Qiu, Broadband near‐IR photoluminescence in Ni^{2+} doped gallium silicate glass–ceramics, J. Mater. Sci. : Mater. Electron. 30 (2019) 17715-17724.

[42] Q. Mao, B. Lan, K. Zhou, Crystallization control in Ni^{2+}-doped glass-ceramics for broadband near-infrared luminesce, J. Am. Ceram. Soc. 103 (2020) 2569-2574.

[43] T. Liu, Z. Liu, J. Wu, K. Zhang, H. An, Z. Hu, S. Deng, X. Li, H. Li, Broadband near-infrared persistent luminescence in Ni^{2+}-doped transparent glass-ceramic $ZnGa_2O_4$, New J. Chem. 46 (2022) 851-856.

[44] C. Shen, Y. Zhao, L. Yuan, L. Ding, Y. Chen, H. Yang, S. Liu, J. Nie, W. Xiang, X. Liang, Transition metal ion doping perovskite nanocrystals for high luminescence quantum yield, Chem. Eng. J 382 (2020).

[45] S.M. Kamil, A.A. Abul-Magd, W. El-Gammal, H.A. Saudi, Enhanced optical and structural features of Ni^{2+}/La^{3+}hybrid borate glasses, Spectrochim. Acta, Part A 267 (2022) 120569.

[46] S. Kück, Laser-related spectroscopy of ion-doped crystals for tunable solid-state lasers, Appl. Phys. B 72 (2014) 515-562.

[47] F. Alarab, K. Hricovini, B. Leikert, L. Nicolaï, M. Fanciulli, O. Heckmann, C. Richter, L. Prušakova, Z. Jansa, P. Šutta, J. Rault, P. Lefevre, M. Sing, M. Muntwiler, R. Claessen, J. Minár, Photoemission study of pristine and Ni-doped $SrTiO_3$ thin films, Phys. Rev. B 104 (2021) 165129.

[48] R.K. Singhal, S. Kumar, Y.T. Xing, U.P. Deshpande, T. Shripathi, S.N. Dolia, E. Saitovitch, Electronic structure and magnetization correlations in Ni doped ZnO, Mater. Lett. 65 (2011) 1485-1487.

[49] R. Hari Krishna, B.M. Nagabhushana, H. Nagabhushana, D.L. Monika, R. Sivaramakrishna, C. Shivakumara, R.P.S. Chakradhar, T. Thomas, Photoluminescence, thermoluminescence and EPR studies of solvothermally derived Ni^{2+} doped $Y(OH)_3$ and Y_2O_3 multi-particle-chain microrods, J. Lumin. 155 (2014) 125-134.

[50] K. Zhou, S. Zhao, P. Wu, J. Xie, EPR parameters and spectral fine structure of Ni^{2+} in $LiNbO_3$, Phys. stat. sol.(b) 162 (1990) 193.

[51] P.J. Alonso, R. Alcala, J.M. Spaeth, Ni^{2+} ions in $RbCdF_3$: An EPR study in the cubic and tetragonal phases, Phys. Rev. B 41 (1990) 10902-10905.

[52] W.L. Feng, X.M. Li, W.J. Yang, C.Y. Tao, Y.L. Yang, Optical absorption spectra and EPR g factor of divalent nickel doped magnesia crystal, Optik 122 (2011) 1512-1514.

[53] X. Qin, D.-S. Deng, W.-L. Feng, Substitutional site and defect structure of Ni^{2+} in $YAlO_3$ nanophosphor studied from the optical and electron paramagnetic resonance spectra, Radiat. Eff. Defects Solids 172 (2017) 187-191.

[54] L. Yuan, Y. Jin, C. Zhu, Z. Mou, G. Xie, Y. Hu, Ni^{2+}-doped yttrium aluminum gallium garnet phosphors: Bandgap engineering for broad-band wavelength-tunable shortwave-infrared long-persistent luminescence and photochromism, ACS Sustainable Chem. Eng. 8 (2020) 6543-6550.

[55] O.S. Dymshits, A.A. Zhilin, T.I. Chuvaeva, M.P. Shepilov, Structural states of Ni(II) in glasses and glass-ceramic materials of the lithium-aluminium-silicate system, J. Non-Cryst. Solids 127 (1991) 44-52.

[56] V. Džimbeg-Malčić, Ž. Barbarić-Mikočević, K. Itrić, Kubelka-Munk theory in describing optical properties of paper (II), Teh. vjesn. 19 (2012) 191-196.

[57] Y. Zhuang, J. Ueda, S. Tanabe, P. Dorenbos, Band-gap variation and a self-redox effect induced by compositional deviation in $Zn_xGa_2O_{3+x}$:Cr^{3+} persistent phosphors, J. Mater. Chem. C 2 (2014) 5502-5509.

[58] A. Escobedo Morales, E. S´anchez Mora, U. Pal, Use of diffuse reflectance

spectroscopy for optical characterization of un-supported nanostructures, Rev. Mex. Fis. S 53 (2007) 18-22.

[59] S. Lany, A. Zunger, Assessment of correction methods for the band-gap problem and for finite-size effects in supercell defect calculations: Case studies for ZnO and GaAs, Phys. Rev. B 78 (2008) 235104.

[60] G. Williams, B. Seger, P.V. Kamat, TiO_2-graphene nanocomposites. UV-assisted photocatalytic reduction of graphene oxide, ACS Nano 2 (2008) 1487-1491.

[61] K. Li, D. Xue, Estimation of electronegativity values of elements in different valence states, J. Phys. Chem. A 110 (2006) 11332-11337.

[62] H. Wu, Q. Zhu, X. Sun, J.-G. Li, Regulating anti-site defects in $MgGa_2O_4:Mn^{4+}$ through Mg^{2+}/Ge^{4+} doping to greatly enhance broadband red emission for plant cultivation, J. Mater. Res. Technol. 13 (2021) 1-12.

[63] J. Xu, S. Tanabe, Persistent luminescence instead of phosphorescence: History, mechanism, and perspective, J. Lumin. 205 (2019) 581-620.

[64] T. Si, Q. Zhu, T. Zhang, X. Sun, J.-G. Li, Co-doping Mn^{2+}/Cr^{3+} in $ZnGa_2O_4$ to fabricate chameleon-like phosphors for multi-mode dynamic anti-counterfeiting, Chem. Eng. J. 426 (2021) 131744.

[65] X. Teng, W. Zhuang, H. He, Influence of La^{3+} and Dy^{3+} on the properties of the long afterglow phosphor $CaAl_2O_4:Eu^{2+},Nd^{3+}$, Rare Met. 27 (2008) 335-339.

[66] X. Lu, W. Shu, Roles of crystal defects in the persistent luminescence of Eu^{2+}, Dy^{3+} co-doped strontium aluminate based phosphors, Rare Met. 26 (2007) 305-310.

[67] K.V.d. Eeckhout, P.F. Smet, D. Poelman, Persistent luminescence in Eu^{2+}-doped compounds: A Review, Materials 3 (2010) 2536-2566.

[68] S. Zhou, N. Jiang, H. Dong, H. Zeng, J. Hao, J. Qiu, Size-induced crystal field parameter change and tunable infrared luminescence in Ni^{2+}-doped high-gallium nanocrystals embedded glass ceramics, Nanotechnol. 19 (2008) 015702.

[69] J. Nie, Y. Li, S. Liu, Q. Chen, Q. Xu, J. Qiu, Tunable long persistent luminescence in the second near-infrared window via crystal field control, Sci. Rep. 7 (2017).

[70] W.C. Wang, R. Zhou, H.Q. Le, Q.Y. Zhang, L. Wondraczek, Ni-doped fluorosulfates with broad NIR luminescence, J. Lumin. 210 (2019) 457-463.

Supporting Information

A new persistent luminescence phosphor of $ZnGa_2O_4:Ni^{2+}$ for the second near-infrared transparency window

Minghui Jin[1], Fan Li[1], Junqing Xiahou[1], Lin Zhu[2], Qi Zhu[1*] and Ji-Guang Li[3]

[1]*Key Laboratory for Anisotropy and Texture of Materials (Ministry of Education), School of Materials Science and Engineering, Northeastern University, Shenyang, Liaoning 110819, PR China*

[2]*College of Sciences, Northeastern University, Shenyang Liaoning 110819, PR China*

[3]*Research Center for Functional Materials, National Institute for Materials Science, Namiki 1-1, Tsukuba, Ibaraki 305-0044, Japan*

[*]Corresponding author:

Dr. Qi Zhu (Professor)

Tel: +86-24-8367-2700

E-mail: zhuq@smm.neu.edu.cn

Table S1 The acronyms of the words.

	acronyms
near-infrared	NIR
ultraviolet	UV
visible	VIS
aggregation-induced-emission	AIE
X-ray diffraction	XRD
X-ray photoelectron spectroscopy	XPS
electron paramagnetic resonance	EPR
photoluminescence excitation	PLE
photoluminescence	PL
thermo-luminescence	TL
conduction band	CB
electronegativity	EN
valence band	VB
conduction band bottom	CBB
diffuse reflectance	DR
charge transfer	CT